IEEE Access
Multidisciplinary ⋮ Rapid Review ⋮ Open Access Journal

Received 1 May 2025, accepted 14 May 2025, date of publication 19 May 2025, date of current version 27 May 2025.

Digital Object Identifier 10.1109/ACCESS.2025.3571376

RESEARCH ARTICLE

Enhancing Fault Detection and Localization in MT-MVDC Networks Using Advanced Singular Spectrum Analysis

HOSSAM SABRA[1], AMR KASSEM[2], AHMED A. A. ALI[2], (Member, IEEE), KARAM M. ABDEL-LATIF[2], AND AHMED F. ZOBAA[3], (Senior Member, IEEE)
[1]South Cairo Electricity Distribution Company, Ministry of Electricity and Energy, Cairo 11841, Egypt
[2]Department of Electrical Machine and Power Engineering, Faculty of Engineering, Helwan University, Cairo 11795, Egypt
[3]College of Engineering, Design and Physical Sciences, Brunel University of London, UB8 3PH Uxbridge, U.K.

Corresponding author: Ahmed F. Zobaa (azobaa@ieee.org)

ABSTRACT This paper presents a novel methodology for fault detection, classification, and localization in Multi-Terminal Medium Voltage Direct Current (MT-MVDC) networks. The proposed approach utilizes Singular Spectrum Analysis (SSA) to decompose measured positive and negative pole voltages, isolating the seasonal component that represents the traveling wave. Fault detection is based on comparing this component against a predefined threshold, where minimal fluctuations occur under normal conditions, but significant variations emerge after a fault. Fault classification is achieved by analyzing the rate of change of the line-mode current to distinguish between forward and backward faults. For fault localization, the method leverages traveling wave attenuation and dispersion. The first traveling wave is extracted from the voltage seasonal component, and its spreading behavior over distance is analyzed to compute the curvature rate, enabling precise fault location estimation. The methodology is validated through extensive simulations on an MT-MVDC distribution system using PSCAD/EMTDC. MATLAB is employed for signal processing, and the approach is tested under various fault scenarios, including high fault impedance and extreme external faults. Comparative analysis with existing methods highlights the advantages of the proposed technique in terms of accuracy and robustness.

INDEX TERMS MVDC distribution network, intelligent electronic device (IED), fault detection, fault location, singular spectrum analysis (SSA).

I. INTRODUCTION

MT-MVDC networks facilitate the interconnection of multiple terminals, including renewable energy sources and microgrids, offering significant improvements in power system efficiency, reliability, and operational flexibility. However, ensuring the stable operation of these networks requires precise fault detection, location, and isolation to maintain system reliability and minimize downtime.

In DC networks, fault development is characterized by a rapid current surge due to capacitor discharge. To mitigate this, the insulated-gate bipolar transistor (IGBT) is blocked, halting further current flow. Subsequently, a diode freewheeling phase occurs, during which the stored energy in the line inductance dissipates [1]. To prevent damage to freewheeling diodes, effective DC protection schemes must ensure fast fault detection and precise fault localization. Accurate identification of faulted lines enables targeted isolation, while precise location information facilitates rapid system restoration.

Fault detection schemes for MT-MVDC networks can be categorized into voltage and current protection, boundary protection, pilot protection, and traveling wave protection. Various strategies, including overcurrent, undervoltage, phased overcurrent/current rate-of-change, and voltage rate-of-change methods, have been proposed in [2], [3], and [4].

The associate editor coordinating the review of this manuscript and approving it for publication was Binit Lukose.

While effective for single-terminal systems, these approaches may lack selectivity in multiterminal networks and struggle with large transition resistances.

Single-ended protection schemes, widely used in high-voltage direct current (HVDC) systems, are less effective in MVDC networks due to the absence of boundary elements (line reactors), which are rarely installed even at converter terminals [5]. While line reactors aid fault detection and location, their absence presents a key challenge for MVDC protection design.

Pilot protection offers a more robust alternative for DC distribution, ensuring effective zone-based protection. Pilot protection is divided into directional pilot protection and current differential protection. The former identifies faults based on triggered events using electrical quantities at both line ends, while the latter compares currents at both ends of the protected element. References [6], [7], [8], and [9] explore current differential protection methods using both time-domain and frequency-domain analysis. Additionally, event-based protection schemes utilizing communication infrastructure and transient fault current derivatives have been introduced in [10] and [11].

Traveling wave-based detection enables rapid fault identification due to the near-speed-of-light propagation of traveling waves, making it well-suited for DC protection schemes that require swift response times to protect freewheeling diodes. This method provides comprehensive fault information through single-ended or double-ended configurations, with its accuracy heavily dependent on the signal processing techniques used for feature extraction.

Reference [12] proposes a high-speed fault detection method for MVDC networks using the Extended Kalman Filtering Algorithm, though it lacks analysis of noise impact and is limited to a fault resistance of 50 ohms. Techniques such as Short-Time Fourier Transform (SFFT) [13] and Fast Fourier Transform (FFT) [14] offer fast computation but struggle with time-frequency resolution, while Hilbert-Huang Transform (HHT) [15] improves adaptability but is constrained by intrinsic mode function (IMF) selection. Reference [16] introduces a non-unit traveling wave protection method using Discrete Wavelet Transform (DWT) to analyze high-frequency components of voltage traveling waves.

Advanced methods, including Variational Mode Decomposition (VMD) and the S-Transform (ST) [17] and [18], enhance fault detection but remain sensitive to noise. While the S-Transform provides high time-frequency resolution, it requires adaptive parameter tuning [18]. Noise interference remains a challenge for both VMD and the S-Transform, potentially affecting fault detection accuracy. Reference [19] combines singular value decomposition (SVD) and empirical mode decomposition (EMD) for arc fault localization, though its computational complexity challenges real-time application.

While traveling wave-based methods enable rapid fault detection, their practical implementation faces several challenges. Noise sensitivity is a significant issue, as conventional signal processing techniques, such as FFT and HHT, often struggle to mitigate noise, reducing detection accuracy in noisy environments, as stated in [20]. High Impedance Faults (HIFs) present another challenge, as their weak fault signatures can be misinterpreted as normal transient disturbances [21], [22]. Additionally, the dispersed energy distribution of HIFs further complicates detection. In multi-terminal systems, wave interactions, including reflections and refractions, can obscure fault identification. These challenges underscore the need for more robust and adaptive signal processing techniques to improve fault detection reliability in MVDC networks.

The proposed fault detection methodology, based on the SSA technique, overcomes the limitations associated with conventional traveling wave-based approaches in MT-MVDC networks. SSA is an advanced time-series decomposition method that partitions the measured signal into three distinct components: trend, seasonal, and noise. This study demonstrates that applying the SSA algorithm for fault detection effectively addresses key limitations of existing traveling wave-based methods, as outlined below:

- Noise Reduction: SSA efficiently isolates noise components, enhancing fault detection robustness even in noisy environments.
- Cyclic Pattern Identification: The seasonal component captures cyclic patterns of traveling waves, improving the detection of fault events, including high-impedance faults.
- Trend Isolation: The trend component distinguishes long-term variations, such as normal load fluctuations, from fault-induced disturbances.
- Simplicity and Robustness: Unlike many advanced signal processing techniques, SSA does not require adaptive adjustments or parameter tuning, simplifying implementation.
- Threshold Determination: The clear separation of signal components facilitates threshold selection, making the method adaptable to various test scenarios and practical applications.

However, SSA remains relatively unexplored in transient condition protection schemes and is not yet widely adopted in the field.

On the other hand, to improve system restoration time, various fault location techniques have been employed in DC systems, including model-based methods, knowledge-based approaches, and traveling wave-based techniques.

Model-based methods, such as the approach in [23], utilize an estimated R-L representation of transmission lines for fault location. However, their accuracy is highly sensitive to variations in line parameters, such as resistance and inductance, which can change due to environmental conditions or aging. Additionally, these methods require precise system modeling and parameter estimation, limiting their adaptability in real-world scenarios with uncertain or fluctuating line characteristics.

Recent research has explored machine learning (ML) to enhance fault location strategies. For example, [24] integrates artificial neural networks with wavelet transforms, while [25] employs a feature matrix combined with a long short-term memory (LSTM) model. Although ML-based methods offer promising advancements, they are affected by data quality and generalization challenges in diverse network configurations. Moreover, their complexity can reduce interpretability and increase computational costs.

Traveling wave-based techniques determine fault locations by detecting and analyzing traveling waves. For instance, [26] applies a first-order high-pass Butterworth filter to identify wave polarity and timing, while [27] enhances wave peak differentiation using a high-pass filter. Reference [28] introduces a double-ended traveling wave method that leverages the linear relationship between wave time differences and fault location. Additionally, [29] utilizes Variational Mode Decomposition and the Teager Energy Operator to extract fault features and detect traveling wave arrivals.

Although traveling wave (TW) fault location schemes provide rapid and precise fault detection, they face several key challenges. Both single-ended and double-ended methods are affected by noise interference, variations in wave propagation speed, and interactions between incident and reflected waves [20]. Noise interference is particularly problematic, as fault-induced traveling waves can be obscured by background noise from load fluctuations and measurement inaccuracies. Additionally, accurate fault location depends on precise estimation of wave propagation speed, which can vary due to environmental conditions and cable characteristics [30].

High Impedance Faults (HIFs) further complicate detection, as their weak traveling wave signatures make it difficult to identify wave-fronts, determine arrival times, and differentiate between incident and reflected waves [21], [22]. Moreover, double-ended approaches are highly sensitive to data transmission errors or delays, which can compromise synchronization between line terminals and reduce accuracy. These limitations highlight the need for advanced fault location techniques that improve accuracy and reliability in multiterminal MVDC networks.

To overcome the limitations of existing traveling wave-based fault location techniques, this study introduces a novel approach that integrates Singular Spectrum Analysis (SSA) to enhance fault detection and localization in MT-MVDC networks. The decomposition capabilities of SSA provides several advantages. First, it effectively isolates noise from trend and seasonal components, improving robustness against measurement inaccuracies. Second, it enhances traveling wave detection, even in high-impedance fault scenarios, as the seasonal component captures the cyclic patterns characteristic of traveling waves. Additionally, the proposed method eliminates dependence on traveling wave arrival time and propagation speed, addressing key challenges of conventional fault location techniques.

The proposed approach applies SSA to voltage measurements for fault identification and localization. Fault detection is achieved by comparing the extracted seasonal component against a predefined threshold. To determine fault location, the method leverages traveling wave attenuation and dispersion, analyzing the relationship between the initial wave propagation and fault distance within a specified time window. Notably, the approach does not require synchronization, ensuring accurate fault localization. It effectively detects faults with resistances up to 200 Ω, demonstrating its robustness. Furthermore, the method is independent of specific grid configurations, making it adaptable to various network topologies.

This paper is structured as follows: Section I presents an overview of fault detection and location methods in MT-MVDC distribution networks, highlighting their limitations. Section II describes the MT-MVDC network test model used in the study. Section III analyzes the structure of the singular spectrum analysis approach and outlines the step-by-step procedure for fault identification and location. Section IV examines the simulation results for fault identification and location under various scenarios and compares them with existing methods. Section V summarizes the key findings and contributions of the study.

II. MULTI-TERMINAL MVDC NETWORK

The 33-kV MT-MVDC network, illustrated in Figure 1, was modeled using the PSCAD/EMTDC platform. This network employs a unipolar symmetric bus structure with a low-resistance grounded DC capacitor neutral point, where each pole operates at 16.5 kV. The system comprises six DC buses interconnected by five pairs of 18/30 kV XLPE single-core cables. Bus 1 and Bus 4 are connected to AC networks 1 and 2 via 50 MVA Voltage Source Converter (VSC) units (VSC1 and VSC2), respectively. Bus 3 interfaces with a DC load through a DC-DC converter and connects to a microgrid via a DC-AC converter. The microgrid includes inverter-based distributed generation (DG) units, which contribute limited fault currents, typically capped at 120% of their rated full-load current. In grid-connected mode, these DG units operate in constant power mode, injecting a fixed amount of power into the network. Additionally, an AC load is connected to the system via a DC-AC converter at Bus 5, and a wind farm interfaces with Bus 5 through an AC-DC converter.

To simplify control strategies and modelling, a two-level voltage source converter will be employed for the test system This choice is justified as the fault current characteristics remain consistent across various DC topologies, including two-level, three-level, and Modular Multi-level Converters (MMC). The MVDC network utilizes a vector control mechanism, comprising a Phase-Locked Loop (PLL) Controller, an Inner Loop Controller, and an Outer Loop Controller. To ensure the stability and reliability of the MVDC network, VSC1, connected to AC grid 1, is assigned the primary role of

DC voltage regulation. VSC2, on the other hand, is primarily responsible for active power flow control. In the event of an outage in AC grid 1, VSC2 assumes the role of DC voltage regulation to maintain system stability. Table 1 provides a detailed overview of the control strategies implemented for each VSC.

In the following section, a novel fault detection and location technique is proposed to address the limitations highlighted in Section I. The proposed technique will be demonstrated through simulations on the MT-MVDC network depicted in Figure. 1

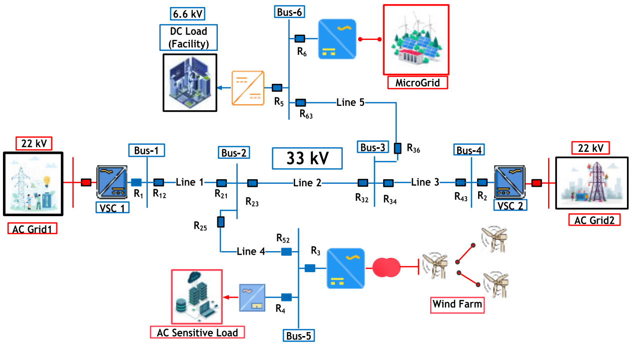

FIGURE 1. MVDC network.

TABLE 1. MVDC network data.

System Voltage	DC Network			33 kV / ±16.5 kV
	AC grid			22 kV
	AC load			22 kV, P=40MW, Q=4 MVAR
	DC load			6.6 kV, P = 14 MW
Converter Stations	Name	Rated Voltage	Bus	Operation mode
	VSC-1	33 kV	1	Q=2 MVAR, Vdc =33 kV
	VSC-2	33 kV	4	P=30 MW, Q = Q=2 MVAR
	AC-DC	33 kV	5, 6	P=20 MW, Q =0
	DC-AC	33 kV	5	Vac =22kV, Q=4MVAR
	DC-DC	33/6.6 kV	6	P=12 MW, Q=0
Cable Data	R= 0.0176 Ω/km L= 0.3387 mH/km		Cables 1, 3	7 km
	C=0.44 µF/km Surge impedance 15.5 Ω		Cables 2, 4, 5	5 km

III. PROPOSED FAULT IDENTIFICATION & LOCATION SCHEME FOR MVDC NETWORK

In this section, a novel scheme for fault detection and location in MVDC networks is presented. The framework of DC fault current was previously examined by the authors in [11], enabling the development of an effective fault protection scheme. Initially, an analysis of SSA is conducted. SSA has been effectively applied across various domains. Reference [31] uses SSA to preprocess electric load data by removing high-frequency noise, enhancing input quality for Long Short-Term Memory (LSTM) models in load forecasting. Reference [32] applies SSA to decompose stator current signatures, enabling fault detection in induction machines under low slip conditions. Reference [33] proposes an SSA-based method for fault detection in rolling element bearings by constructing a baseline feature space from healthy signals for comparison with new data.

The proposed scheme, which follows a step-by-step procedure to facilitate fault identification and precise pinpointing of fault locations, is then illustrated.

A. SINGULAR SPECTRUM ANALYSIS

The SSA method, introduced by Broomhead and Gregory in 1986 [34], has demonstrated remarkable efficacy across various practical domains. Its applications include identifying underlying data structures, extracting periodic patterns and intricate trends, as well as facilitating data smoothing and detecting change points [35]. SSA is a versatile technique used in decomposing a time series data into its underlying components, such as trend, seasonal, and residual. To streamline the SSA procedure, the following step is introduced:

Stage 1: Decomposition

a) Embedding: transform the one-dimensional time series Y into a multi-dimensional series to form a trajectory matrix. The embedding step can be described as follows: Given a time series $Y = (y_1, y_2, \ldots\ldots, y_N)$ of length N, the number of lagged vectors K is defined within the range [3, N/2], where N is the length of the input data, and the window length L is computed as $L=N-K+1$. The formed trajectory matrix [X] containing lagged vectors is expressed as follow:

$$X = \begin{bmatrix} x_1 & x_2 & \ldots & x_K \\ x_2 & x_3 & \ldots & x_{K+1} \\ \vdots & \vdots & \ddots & \vdots \\ x_L & x_{L+1} & \ldots & x_N \end{bmatrix} \tag{1}$$

b) IEEE will do the final formatting of your paper. If your paper is intended for a conference, please observe the conference page limits. Singular Value Decomposition (SVD) is a powerful mathematical tool used in linear algebra for analyzing and simplifying complex datasets. SVD has broad applications, including dimensionality reduction, which is used in data compression, and noise reduction. It decomposes a given matrix into three distinct components: two orthogonal matrices and a diagonal matrix of singular values. As follow: The general Form of SVD is as follow:

$$\begin{aligned} &\begin{bmatrix} x_1 & x_2 & \ldots & x_K \\ x_2 & x_3 & \ldots & x_{K+1} \\ \vdots & \vdots & \ddots & \vdots \\ x_L & x_{L+1} & \ldots & x_N \end{bmatrix} \\ &= \begin{bmatrix} u_{11} & u_{12} & \cdots & u_{1L} \\ u_{12} & u_{22} & \cdots & u_{2L} \\ \vdots & \vdots & \ddots & \vdots \\ u_{L1} & u_{L2} & \ldots & u_{LL} \end{bmatrix} \times \begin{bmatrix} \sigma_1 & \ldots & \cdots & 0 \\ 0 & \sigma_2 & \cdots & 0 \\ \vdots & \vdots & \ddots & \vdots \\ 0 & 0 & \ldots & \sigma_r \end{bmatrix} \\ &\times \begin{bmatrix} v_{11} & v_{12} & \ldots & v_{1K} \\ v_{12} & v_{22} & \ldots & v_{2K} \\ \vdots & \vdots & \ddots & \vdots \\ v_{K1} & v_{K2} & \ldots & v_{KK} \end{bmatrix}, \end{aligned} \tag{2}$$

where:

[U]: An (L x L) orthogonal matrix whose columns are the left singular vectors of [X]

[Σ]: An (L x K) diagonal matrix containing the singular values of [X], which are non-negative real numbers sorted in descending order.

[V^T]: is the transposed matrix of an (K × K) orthogonal matrix [V] whore the columns represent the right singular vectors of [X].

The SVD process sorts decomposition matrices in descending order of singular values, with the largest singular values and their corresponding eigenvectors in (U) and (V^T) representing the most significant principal components, used to construct the trend component.

Stage 2: Reconstruction

c) Group Eigenvectors: After performing SVD, the eigenvectors (columns of U and V) are grouped based on their singular values. Each group represents components of the time series with similar patterns. Let {G1, G2…, Gm} denote the disjoint subsets of eigenvectors. The grouping process involves summing the matrices corresponding to each subset as in (3) to form:

$$X_{Gi} = \sum\nolimits_{j\in Gi} \sigma_i u_i v_i^T \tag{3}$$

Each XGi represents a component of the time series, such as trend or seasonality.

The grouping step entails the process of clustering similar eigenvectors following the decomposition of the trajectory matrix through SVD. After the SVD, the eigenvectors are arranged in accordance with their corresponding singular values, facilitating the identification of clusters or groups of eigenvectors that represent analogous patterns or components within the time series.

d) Average Along Diagonals: Calculate the diagonal averages to obtain the time series component for each group. The k-th term of the reconstructed time series component, $y_k^{(Gi)_i}$, for matrix X_{Gi}, is calculated using (4)

$$y_k^{(Gi)} = \frac{1}{d_k} \sum\nolimits_{i+j=k+2} x_{i,j}, \tag{4}$$

where, dk is the number of terms contributing to the k-th diagonal.

e) Reconstruct Time Series Components: Summarize the components obtained from diagonal averaging as in (5):

$$yk = \sum\nolimits_{i=1}^{m} y_k^{(Gi)}, \tag{5}$$

where y_k represents the k-th term of the overall reconstructed time series.

To illustrate the decomposition of voltage signals using SSA, Fig. 2(a-d) depict the simulated line-mode voltage, trend component, seasonal component, and residual noise at IED12, respectively. A fault is simulated at 0.2 s on Line 1, 4 km away from Bus 1, with a lag value of 3. As shown in the figures, the trend component captures the overall trend of the voltage signal, while the seasonal component isolates the cyclic patterns associated with traveling waves. The residual component comprises the remaining signal components, including noise and other disturbances.

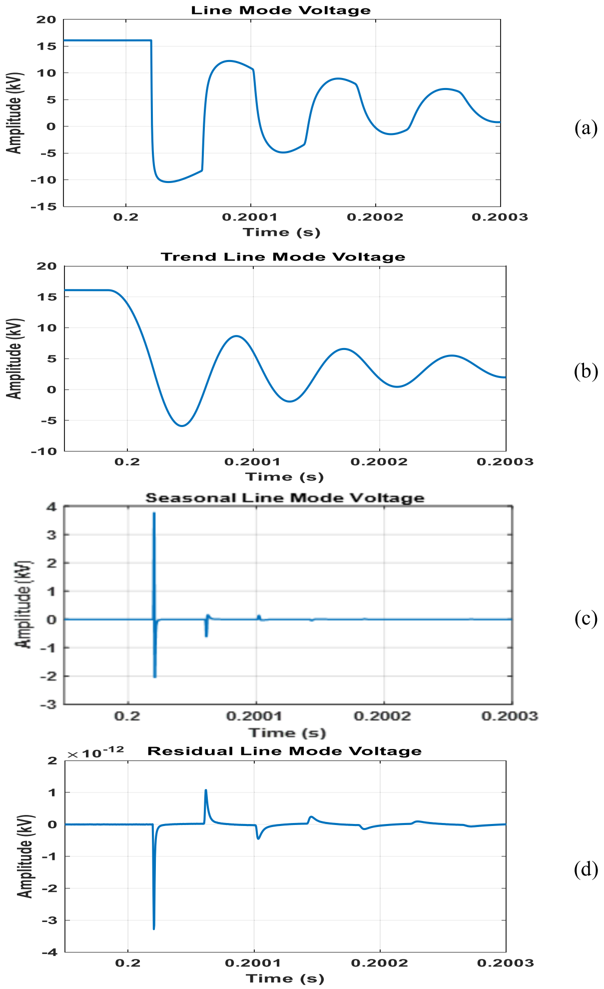

FIGURE 2. SSA decomposition components with lag value of 3.

The trend component corresponds to the slowly varying, non-oscillatory part of the data, identified by examining the leading eigenvectors from the SVD that capture the gradual variations in the time series. The seasonal component, on the other hand, represents the oscillatory patterns not explained by the trend. SSA identifies these patterns by analysing the eigenvectors associated with specific frequencies. The residual component represents the remaining noise or irregular fluctuations after removing the trend and seasonal components. In this analysis, the seasonal component is of particular interest as it represents the traveling waves superimposed on the voltage signal, which arise at the moment of a fault occurrence.

A key parameter in Singular Spectrum Analysis (SSA) is the window length L, which defines the size of the trajectory matrix and significantly influences both the accuracy and computational complexity of the algorithm. The choice of L affects the temporal resolution of the decomposition, impacting the ability of SSA to capture transient features and accurately separate trend, seasonal, and noise components. Given the focus of this study on the transient behavior of traveling waves, special emphasis is placed on extracting the seasonal component. To enhance sensitivity to such transients, the minimum reasonable value in selected, L=3, which ensures the reconstruction of all three components (trend, seasonal, and residual).

To assess the effect of L on decomposition quality, simulations were performed using L=3, L=15, and L=30, as shown in Fig. 3a, 3b, and 3c, respectively. The results indicate that L=3 provides the most accurate representation of the seasonal component, whereas larger values result in smoother trend components but reduced temporal resolution. Furthermore, smaller window lengths improve computational efficiency, reducing both memory usage and execution time. The simulation results indicate that using L=3 yields a fault location error of only 0.14%, compared to 0.25% and 0.37% for L=15 and L=30, respectively. In terms of execution, L=3 runs approximately 25% faster than L=15, and over 40% faster than L=30. Compared to larger L values, the use of L=3 not only enhances fault location accuracy by better capturing transient features but also significantly reduces computational complexity, making it highly suitable for real-time protection applications. This makes the SSA-based approach comparable in computational complexity to the FFT and WT, while being significantly faster than the HHT and VMD. Moreover, the low computational overhead achieved with small window lengths (e.g., L=3) underscores the feasibility of real-time implementation of SSA in practical protection devices equipped with standard microcontrollers.

B. FAULT DETECTION, IDENTIFICATION, LOCATION ALGORITHM

As discussed in the preceding section, the seasonal component of the signal effectively models the cyclical patterns often associated with high-frequency components. These components represent traveling waves that propagate during fault events. By applying SSA to the voltage signal, anomalies indicative of fault conditions can be readily identified. The fault detection, classification, identification, and localization process, illustrated in Fig. 4 as a flowchart, follows these steps:

Step 1- voltage & current measurement: The Intelligent Electronic Device (IED) at the line's head measures both pole voltages and currents.

Step 2- Apply the SSA algorithm: Apply SSA to the both positive and negative pole voltages in order to extract the seasonal component.

Step 3- Fault Detection: Fault detection is achieved when the positive seasonal voltage exceeds the threshold value (ST+ $>$ K) or the negative seasonal voltage falls below the threshold value (ST- $< -$K). The fault is classified based on the pole whose voltage exceeds the threshold.

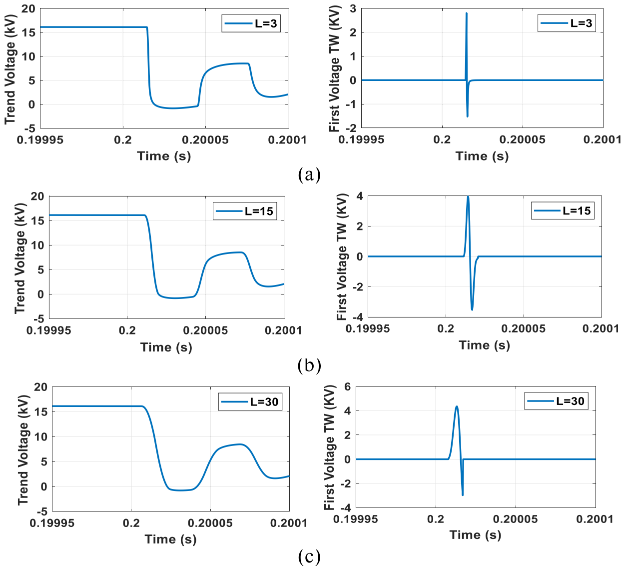

(a)
(b)
(c)

FIGURE 3. **Effect of L value on the SSA decomposition components.**

To determine the optimal threshold value (K) for TW fault detection, a balance must be struck between sensitivity and noise immunity. The threshold must be set sufficiently high to mitigate the effects of measurement noise, while remaining sensitive to low-amplitude TWs that may result from distant, high-resistance faults. Voltage transducers typically maintain a minimum SNR of 50 dB, and commercial protective devices have an error tolerance of ±3%, which influence the choice of threshold value. Additionally, the proposed method, utilizing SSA, further enhances noise isolation by separating noise from the trend and seasonal components. To illustrate this, a positive pole-to-ground fault with a resistance of 200 ohms was introduced at the terminal of Line 1, the longest line in the network. The calculated seasonal component voltage at IED12 is depicted in Fig. 5. Analysis of the results revealed that the lowest detected voltage traveling wave amplitude at IED12 was 66 volts, while the maximum noise level was 11 volts. Consequently, a threshold value of ±20 volts was selected for this study.

Step 4- Identifying Forward or Backward Fault: To distinguish between forward and backward faults, calculate the rate of change of the line mode current using the phase transformation matrix as defined in Equation (6). A forward fault is identified when the rate of change of current (ROCOC) is positive. Conversely, a negative ROCOC indicates the occurrence of a backward fault. This step serves solely for fault direction identification, as fault detection is already achieved in earlier stages—thus, no threshold justification is required here.

$$\begin{bmatrix} X_0 \\ X_1 \end{bmatrix} = \frac{1}{\sqrt{2}} \begin{bmatrix} 1 & 1 \\ 1 & -1 \end{bmatrix} \begin{bmatrix} X_P \\ X_N \end{bmatrix} \tag{6}$$

In this equation, X0 and X1 represent the ground-mode and line-mode voltages or currents, respectively, while XP and

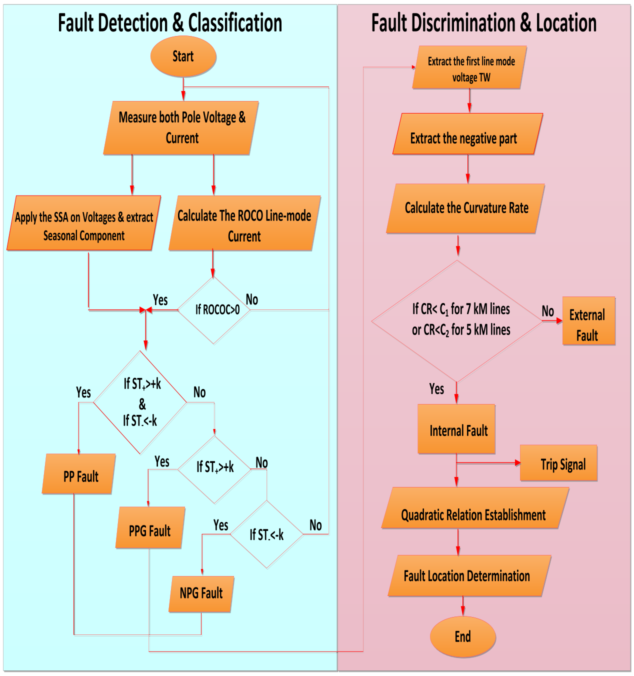

FIGURE 4. Fault detection, classification, and localization scheme chart.

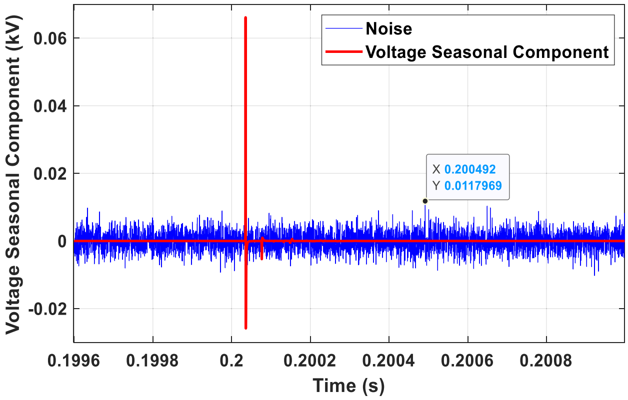

FIGURE 5. Seasonal component of Vtw of IED12 for a 200 Ω PPG fault at $\chi = 7$ km on L1, and with SNR of 50 dB.

XN denote the positive and negative pole voltages or currents, respectively. This transformation effectively reduces the impact of mutual coupling on transient voltage analysis in DC networks.

Step 5- calculate the line mode voltage according to Equation (6) followed by applying SSA algorithm then extract the initial traveling wave by window concept of 10 μs. To illustrate the extraction of the first line-mode traveling wave, a series of pole-to-pole faults with a resistance of 10 ohms were introduced at various locations (0, 1, 2, 3, 4, 5, 6, 7 km) along Line L1 of the system depicted in Figure 1. Both pole voltages were measured and subsequently transformed into line-mode voltage using phase domain transformation. The SSA algorithm was then applied to extract the seasonal component. Finally, a windowing function with a 10 μs duration was employed to isolate the first traveling wave for each fault. Figure 6 presents the extracted first line-mode voltage traveling waves at their respective fault locations.

As depicted in Fig. 6, the first traveling wave undergoes dispersion as it propagates along the transmission line. While no discernible curvature is observed for the 0 km fault, the curve becomes increasingly pronounced and exhibits a higher curvature rate as the fault location moves away from the feeder head. This dispersion phenomenon is particularly evident in the negative portion of the signal. The observed spreading and curvature of the wave are attributed to attenuation and dispersion effects. Attenuation results from energy losses within the line, while dispersion arises from variations in the line's inductance and capacitance, leading to different propagation speeds for various frequency components. The wave velocity along the cable was determined in PSCAD by measuring the arrival times of faults at various locations ranging from 0 to 7 km. The calculated average wave velocity, representing the group velocity, is 1.833 × 108 m/s.

A 10 μs time window was selected to capture the initial traveling wave, considering the maximum dispersion at the furthest fault location across the 7 km line length. This ensures the first wavefront is fully captured. As shown in Fig. 7, the initial transient is successfully recorded even at the maximum distance of 7 km from IED12. A sensitivity analysis confirmed that shorter windows may miss key features, while longer windows introduce reflected components, reducing fault localization accuracy. Therefore, the 10 μs window provides an optimal balance for precise fault location.

Step 6- Extract the negative part: To illustrate the relationship between curvature rate and fault location, five distinct fault types were introduced at a distance of 4 kilometers from IED5 on Line 3: bolted pole-to-pole, pole-to-pole with fault resistances of 10 and 50 ohms, positive pole-to-ground with a fault resistance of 150 ohms, and negative pole-to-ground with a fault resistance of 200 ohms. The negative portion of the extracted traveling waves was isolated and normalized for each fault. Figure 8 illustrates the first line-mode traveling waves for each fault type, while Fig. 9 depicts the normalized negative portions. As observed in the figures, the normalized negative portions remain relatively constant despite variations in fault type and transition resistance.

Step 7- Establish quadratic relation: calculate the summation of the curvature rate by applying differential on the negative part of the initial traveling wave to establish between the curvature rate and the fault location. To elucidate this relationship, a series of fault types were introduced along Line L1 at varying distances from the system origin: bolted pole-to-pole, positive pole-to-ground with a fault resistance of 10 ohm, and negative pole-to-ground with a fault resistance of 150 ohms. The curvature rate of the negative portion of the first line-mode traveling wave voltage was calculated for each fault and plotted against its respective location in Fig. 10. The quadratic coefficients are calculated in MATLAB using

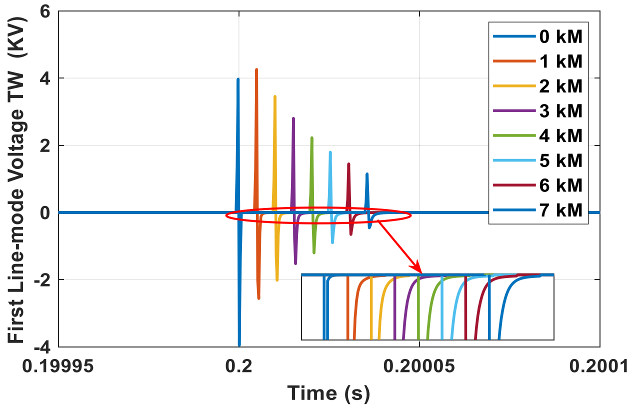

FIGURE 6. Initial traveling waves at different fault distances.

curve-fitting methods that fit a polynomial of a specified degree to the given data points.

Step 8- Faulty section identification, and fault location determination: For each new fault, the curvature rate (CR) is calculated from the normalized negative portion of the initial traveling waves extracted from the line mode voltage using the SSA algorithm. The resulting CR value is then applied to the quadratic relation depicted in Fig. 11 to determine the fault location and classify it as internal or external. For 7 km lines, the CR threshold (C1) is 0.7, while for 5 km lines, it (C2) is 0.6. If the CR falls below the corresponding threshold value, an internal fault is indicated, and a trip signal is sent to the associated circuit breaker.

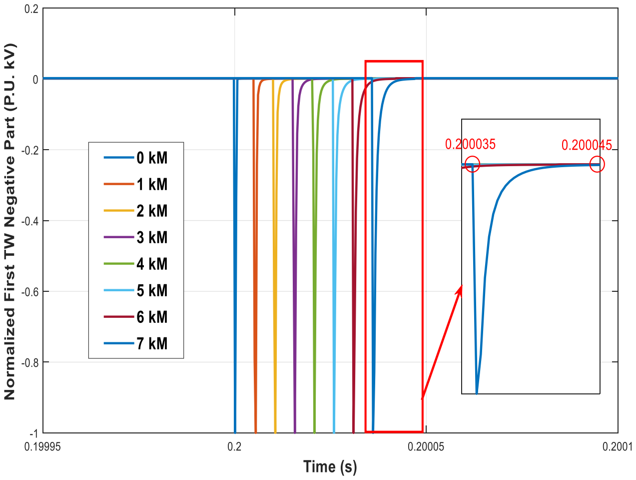

FIGURE 7. Selection of 10 μs window for extracting the first traveling wave.

IV. MODELING, ASSESSMENT, AND VALIDATION

This study examines a multiterminal 33 kV MVDC distribution system (Fig. 1). To evaluate the proposed fault location algorithm, various fault scenarios were simulated using PSCAD. Fault simulations employed a solution step of 0.2 μs and a sampling step of 1 μs. A sampling frequency of 1 MHz is adopted for voltage measurements to ensure precise fault location. While a lower sampling frequency of 25 kHz may suffice for fault detection, a higher sampling rate is essential for accurate time-domain analysis of traveling waves. Notably, commercial protection relays already utilize a sampling frequency of 1 MHz [36], making this approach feasible and practical. Both pole voltages and currents were analyzed in MATLAB to develop the fault detection and location algorithms.

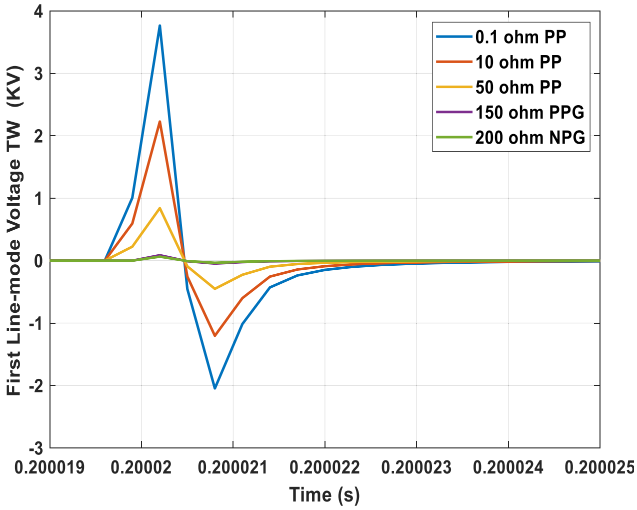

FIGURE 8. Initial traveling waves for different faults at the same fault location.

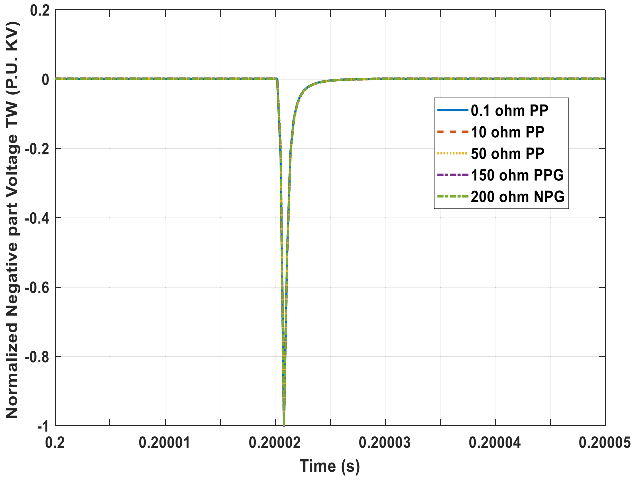

FIGURE 9. Extracted negative part of initial traveling waves for different faults at the same fault location.

A variety of fault types were introduced at different locations, including internal positive pole-to-ground faults to assess algorithm sensitivity and location accuracy, external bolted pole-to-pole faults to evaluate detection security and location accuracy, and negative pole to ground to assess the fault classification and location algorithm. The fault inception time was set to 0.2 s.

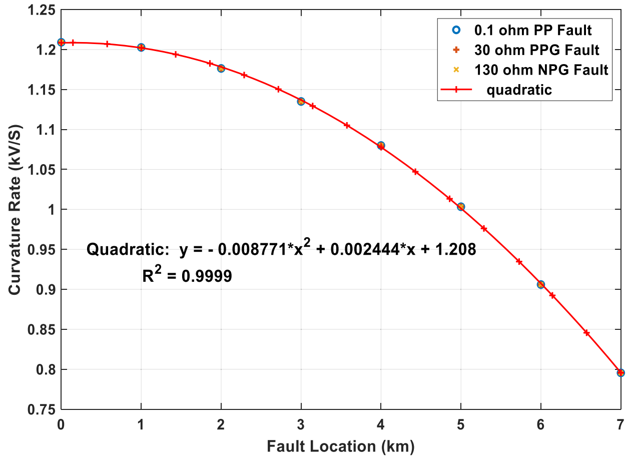

FIGURE 10. Quadratic relation curve between initial TW curvature rate and fault location distance.

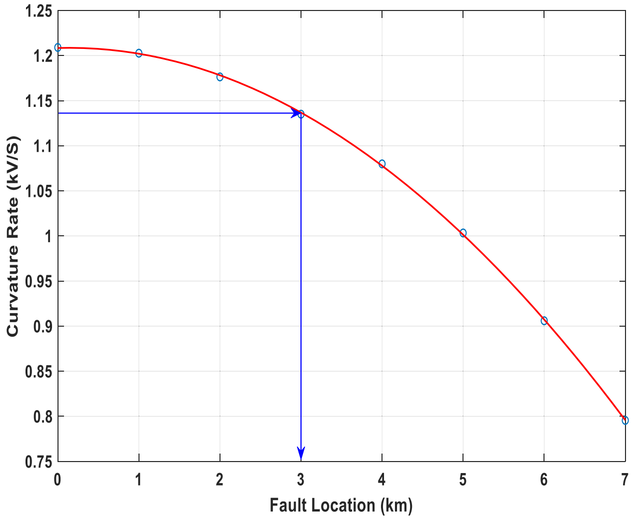

FIGURE 11. Determination of fault location on the quadratic relation.

A. INTERNAL PPG FAULT THROUGH 180 OHMS TRANSITION RESISTANCE ON LINE L1 AT 6.8 KM FROM BUS1

A 180-ohm positive pole-to-ground (PPG) fault was introduced 6.8 km from Bus 1 on Line L1 to assess the detection sensitivity and location accuracy. Fault detection, classification, and localization procedures were performed at both ends of the line, with results presented in Fig. 12. In Step 1, the pole voltages were measured by IED12 and IED21 at both ends, as shown in Figs. 12a and 12b, respectively. In Step 2, the seasonal components were decomposed and compared to threshold values +K and −K, confirming the presence of a positive pole-to-ground fault at IED12 and IED21, as depicted in Figs. 12c and 12d. Step 3 involved calculating the rate of change of current (ROCO) in line mode at IED12 and IED21, which show positive values, confirming a forward fault at both ends, as illustrated in Figs. 12e and 12f. In Step 4, the first traveling wave of the line-mode seasonal voltage was extracted at both IED12 and IED21, as shown in Figs. 12g and 12h. In Step 5, the negative part of the initial traveling wave was extracted at IED12 and IED21, as shown in Figs. 12i and 12j. In Step 6, the curvature rate of the negative part was calculated at both ends and compared to a threshold value (C1 = 0.795378), corresponding to the 7 km line length. Both IEDs confirmed the internal fault and issued a trip command to the associated circuit breakers. In the final Step 7, the curvature rate was projected onto a quadratic curve to determine the fault location. The estimated fault distance was 6804 m from IED12, with an error of 4 m (Fig. 12k), and 197 m from IED21, with an error of 3 m (Fig. 12l).

B. BPP FAULT ON LINE L2 AT 400 M AWAY FROM BUS 3

A bolted pole-to-pole (BPP) fault was introduced 0.4 km from Bus 3 on Line L2 to evaluate detection security and location accuracy. Since IED34 detected a negative rate of change of current (ROCOC), indicating a backward fault, it blocked itself. Fault detection, classification, and localization procedures were carried out for IED43 and IED32, with the results presented in Fig. 7. In Step 1, the pole voltages were measured by IED32 and IED43 at both ends, as illustrated in Figs. 13a and 13b. In Step 2, the seasonal components were decomposed and compared to threshold values +K and −K, confirming the presence of positive and negative pole faults at IED32 and IED43, indicating a pole-to-pole fault, as depicted in Figs. 13c and 13d. Step 3 involved calculating the rate of change of line mode current at IED32 and IED43 are greater than zero, confirming a forward fault at both IEDs, as shown in Figs. 13e and 13f. In Step 4, the first traveling wave of the line-mode seasonal voltage was extracted at both IED32 and IED43, as presented in Figs. 13g and 13h. In Step 5, the negative part of the initial traveling wave was extracted at IED32 and IED43, as shown in Figs. 13i and 13j. In Step 6, the curvature rate (CR) of the negative part was calculated at both ends and compared to threshold values. For IED43, the CR was compared to the threshold value (C1 = 0.795378) corresponding to the 7 km length of Line 3, while for IED32, it was compared to the threshold value (C2 = 1.00097) corresponding to the 5 km length of Line 2. IED43 indicated an external fault as its CR was 0.7458404, which was less than C1, leading it to block itself, while IED32 confirmed an internal fault as its CR was 1.2075744, which exceeded C2, prompting it to send a trip command to the associated circuit breaker. In the final Step 7, the curvature rate was projected onto a quadratic curve to estimate the fault location. The estimated fault distance was 405 m from IED32, with an error of 5 m (Fig. 13k), and greater than 7 km from IED43 (Fig. 13l).

C. NPG FAULT ON LINE L5 AT 3 KM AWAY FROM BUS 3

A negative pole-to-ground (NPG) fault with a 50-ohm fault resistance was introduced 3 km from Bus 3 on Line L5 to evaluate the accuracy of fault classification and location. Fault detection, classification, and localization were performed at both ends of the line, with results shown in Fig. 14.

In Step 1, pole voltages were measured by IED36 and IED63 at both ends, as illustrated in Figs. 14a and 14b. In Step 2, the seasonal components were decomposed and compared to threshold values (+K and −K), confirming negative pole faults at both IED36 and IED63, indicating a negative pole-to-ground fault (Figs. 14c and 14d). In Step 3, the rate of change of current (ROCO) in line mode was calculated at IED36 and IED63 are greater than zero, confirming a forward fault at both ends (Figs. 14e and 14f). In Step 4, the first traveling wave of the line-mode seasonal voltage was extracted at both IED36 and IED63 (Figs. 14g and 14h). Step 5 involved extracting the negative part of the initial traveling wave at IED36 and IED63 (Figs. 14i and 14j). In Step 6, the curvature rate (CR) of the negative part was calculated at both ends and compared to the threshold value (C2 = 1.00097), which corresponds to the 5 km length of Line 5. IED36 indicated an internal fault as its CR was 1.13611, exceeding C2, and IED63 confirmed an internal fault with a CR of 1.17797, also exceeding C2. This prompted both IED36 and IED63 to send a trip command to the respective circuit breakers. Finally, in Step 7, the curvature rate was projected onto a quadratic curve to estimate the fault location. The estimated fault distance was 3006 m from IED36, with an error of 6 m (Fig. 14k), and 1995 m from IED63, with an error of 5 m (Fig. 14l).

D. EXTREME PPG FAULT THROUGH 500-OHM FAULT RESISTANCE ON LINE L1 AT 4 KM FROM BUS1

A positive pole-to-ground (PPG) fault with a fault resistance of 500 ohms was simulated on Line 3 to evaluate the performance of the proposed protection scheme under extreme fault conditions. Protection procedures were executed at both ends of the line, and the results are presented in Fig. 15. In the first step, pole voltages were measured by Intelligent Electronic Devices (IEDs) IED43 and IED34, as shown in Figs. 15a and 15b. The second step involved extracting the seasonal components of the voltage signals and comparing them to predefined thresholds (+K and −K), confirming a positive pole-to-ground fault at both IED43 and IED34 (Figs. 15c and 15d). The rate of change of current (ROCO) was then calculated in the third step, and its positive values confirmed a forward fault at both ends (Figs. 15e and 15f). In the fourth step, the first traveling wave of the line-mode seasonal voltage was extracted at both IEDs (Figs. 15g and 15h), followed by the isolation of its negative component in the fifth step (Figs. 15i and 15j). In the sixth step, the curvature rate of the negative component was computed and compared to a threshold value (C1=0.795378), corresponding to a line length of 7 km. This confirmed the presence of an internal fault, prompting both IEDs to issue trip commands to their respective circuit breakers. Finally, in the seventh step, the curvature rate was projected onto a quadratic curve to estimate the fault location, which was determined to be 4008 m from IED43 with a 8 m error (Fig. 15k) and 2993 m from IED34 with a 7 m error (Fig. 15l). This comprehensive analysis demonstrates the reliability of the proposed protection scheme in identifying and locating faults under extreme high-resistance conditions.

E. ROBUSTNESS TO SUDDEN LOAD CHANGES

In this scenario, a sudden 20 MW AC load is added to the AC side of the DC-AC converter connected to Bus 5 at t = 0.18 s. The resulting line-mode voltage, its trend component, seasonal component, and residual component at IED 52 are depicted in Figure 16a, 156, 16c, and 16d, respectively. The figures indicate that the voltage variation due to the sudden load change is primarily captured by the trend component, with negligible contributions from the seasonal and residual components. This is because the sudden load change results in a gradual adjustment of the system, resulting in smooth variations in current and voltage as the system stabilizes to the new operating point, which is considered a slow variation relative to the SSA algorithm's time scale. In contrast, a short circuit introduces a low-impedance path, causing abrupt and significant increases in current and sharp voltage drops. Consequently, the fault detection scheme is robust to such disturbances.

F. SIMULATION RESULTS AND PERFORMANCE EVALUATION

Extensive simulations demonstrate the effectiveness of the fault location algorithm. The proposed method's effectiveness is demonstrated across three fault types. The maximum detection time for the farthest fault is 175 microseconds, highlighting the scheme's rapid and efficient fault detection capabilities. Simulations confirm the scheme's ability to accurately classify faults as pole-to-pole (PP), positive pole-to-ground (PPG), or negative pole-to-ground (NPG). Moreover, the faulty section is successfully identified by comparing the maximum curvature rate of the line with calculated values. The proposed scheme also effectively pinpoints the fault location by projecting the curvature rate onto the quadratic relation with distance. The results, presented in Table 2, encompass a wide range of DC line faults, including varying types, impedances, and distances. Table 2 demonstrates the method's ability to calculate fault distances for various pole-to-pole, positive-to-ground, and negative pole-to-ground faults. The results show a maximum percentage error of 0.16%.

G. COMPARISON WITH EXISTING FAULT DETECTION AND LOCATION TECHNIQUES

The Several fault detection and location techniques have been proposed in the literature, each with varying performance in terms of accuracy, noise immunity, and hardware requirements. The method presented in [16] employs a line reactor in conjunction with the wavelet transform, achieving a signal-to-noise ratio (SNR) of 25 dB at a sampling frequency of 100 kHz. In contrast, the approach in [14] is limited to low-resistance faults (maximum 10 Ω) and does not consider the effect of noise, which limits its practical applicability.

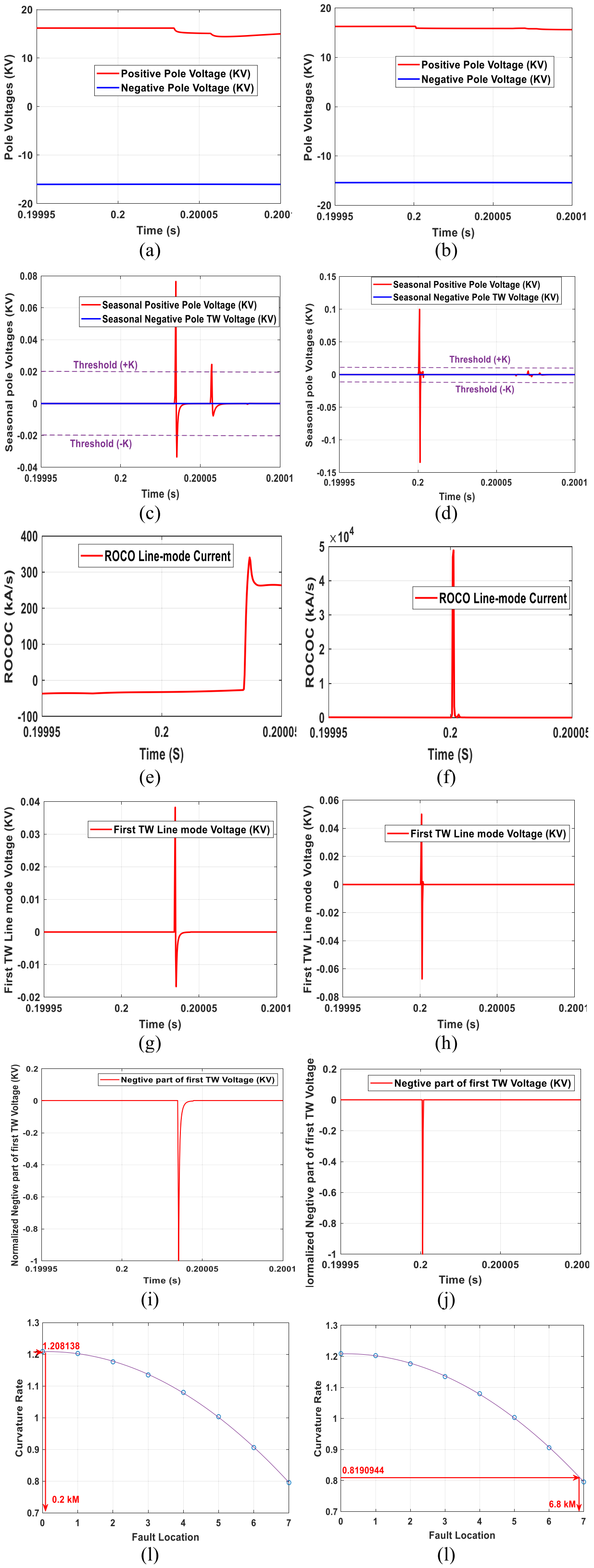

(a) (b)

(c) (d)

(e) (f)

(g) (h)

(i) (j)

(l) (l)

FIGURE 12. PPG fault on Line L1 at 6.8 km away from Bus 1.

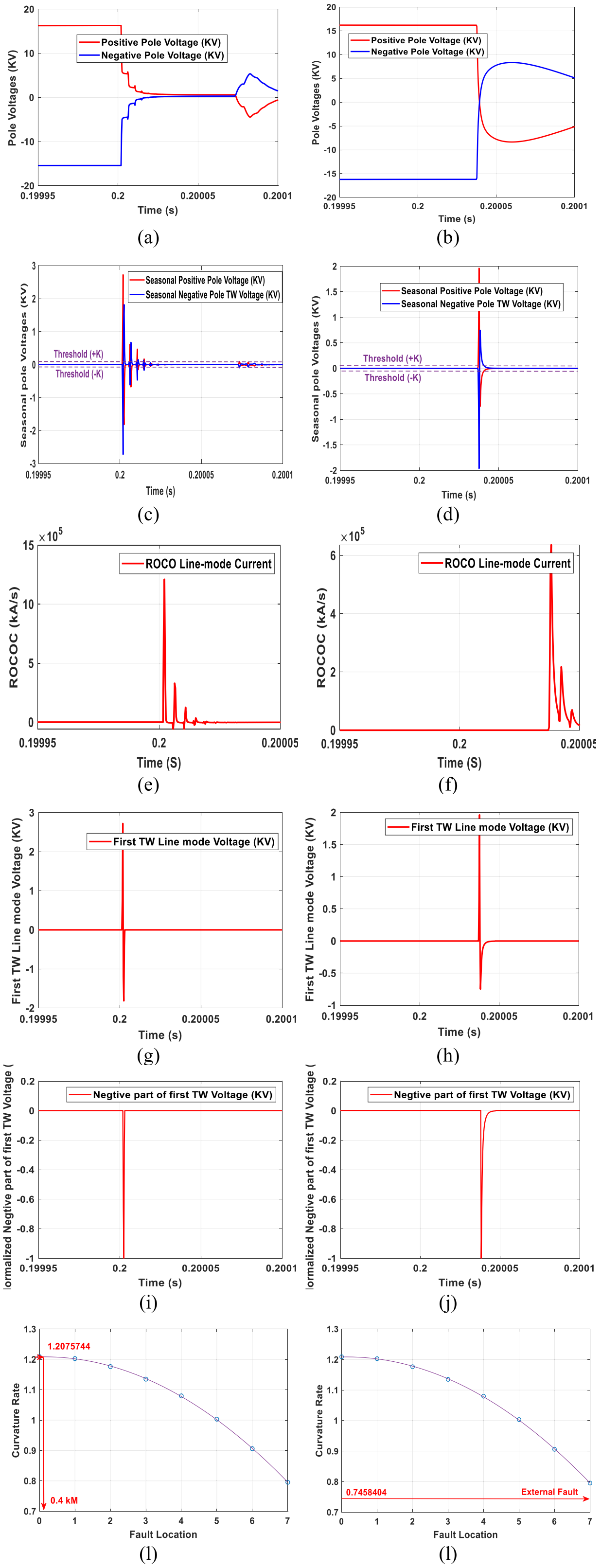

(a) (b)

(c) (d)

(e) (f)

(g) (h)

(i) (j)

(l) (l)

FIGURE 13. Bolted PP fault on Line L2 at 400 m away from Bus 3.

The proposed method significantly improves upon these limitations. It does not require line reactors, is robust to noise up to 50 dB, and achieves ultra-fast fault detection within 0.5 milliseconds. Fault detection is performed effectively

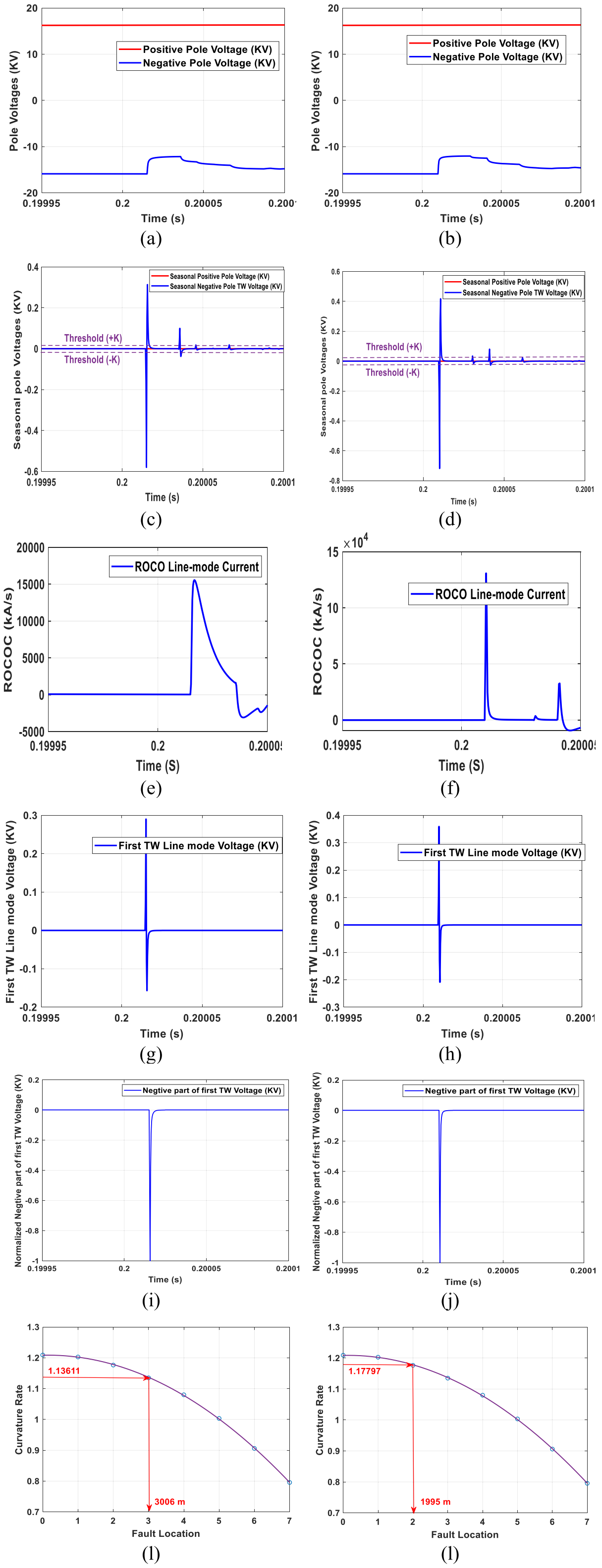

FIGURE 14. NPG fault on Line L5 at 3 km away from Bus 3.

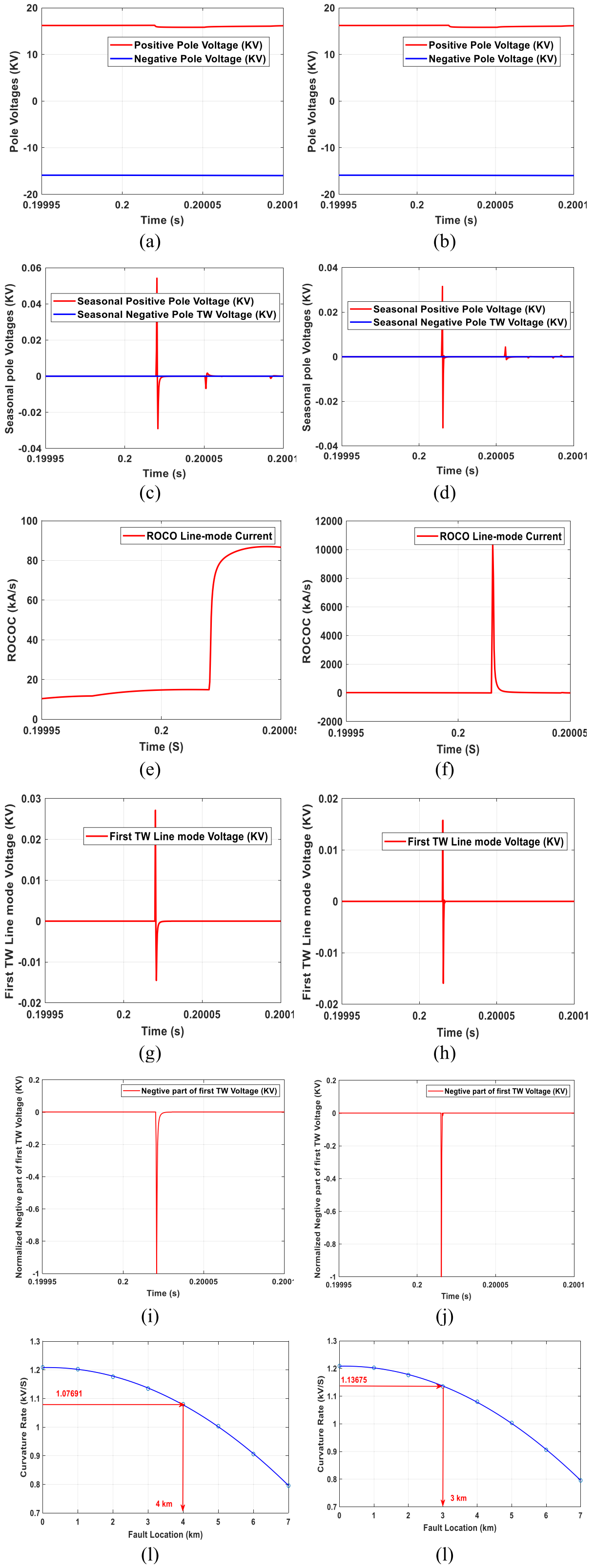

FIGURE 15. NPG fault on Line L5 at 3 km away from Bus 3.

with a sampling frequency of 50 kHz using the SSA-based technique, while fault location requires a higher sampling rate (1 MHz) to ensure accurate arrival time identification and minimize location error—critical factors for enhancing system reliability and reducing outage duration.

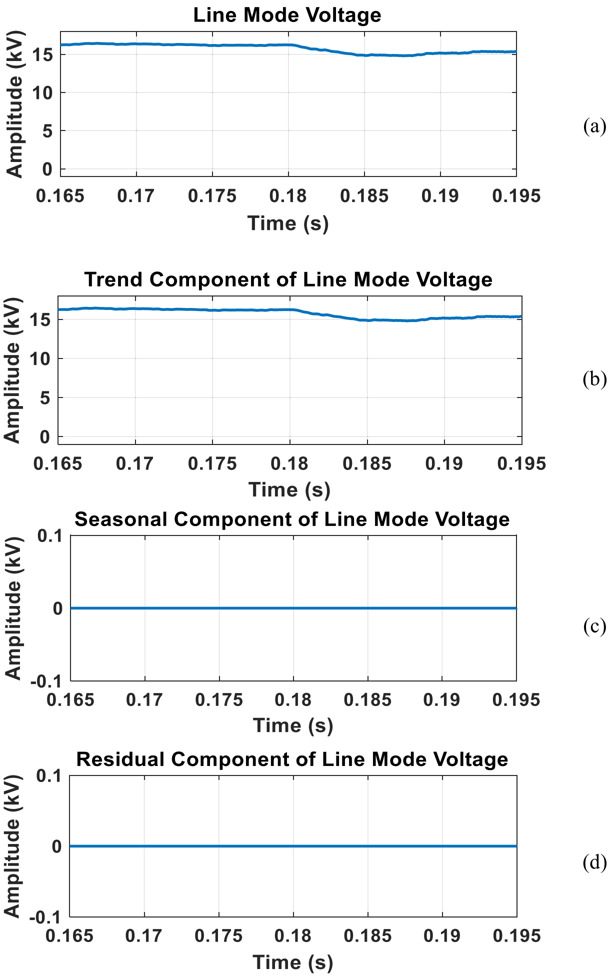

FIGURE 16. Sudden Load change at Bus 5.

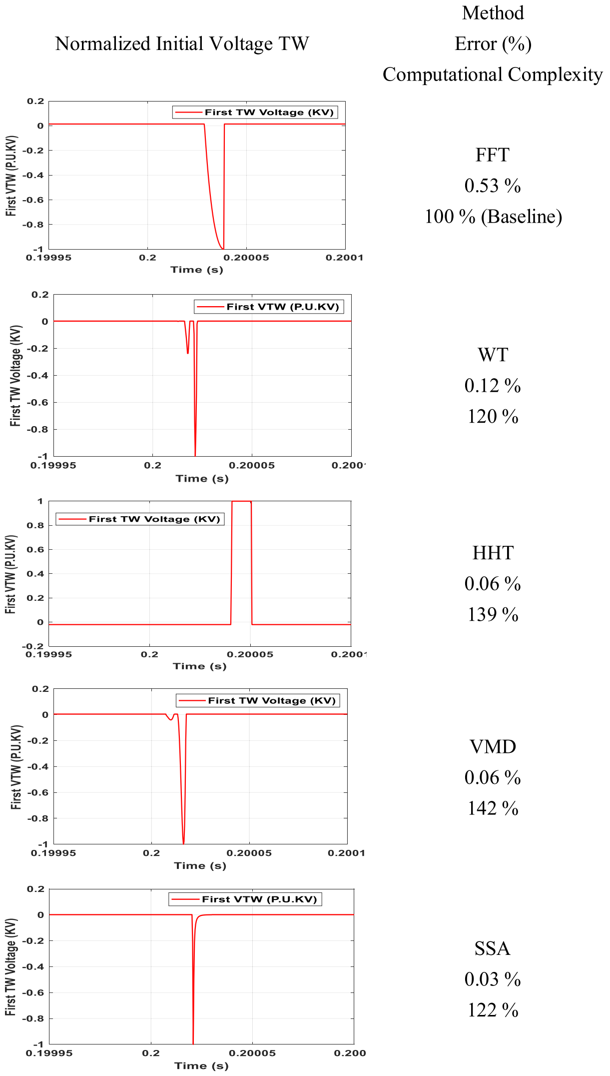

FIGURE 17. Normalized first voltage TW obtained using different signal processing technique.

TABLE 2. Comparison of existing and proposed fault detection and location methods in terms of sampling rate, noise tolerance, and fault resistance handling.

Ref.	Function	Method	Sampling Freq.	Noise (dB)	Max. Fault Resistance (Ω)
[14]	Detection	FFT	–	–	10
[16]	Detection	WT	100 kHz	25	500
[23]	Location	Model-Based	1 MHz	30	500
[27]	Location	HPF	100 kHz	–	500
[28]	Location	WT	1 MHz	–	–
[29]	Location	VMD	1 MHz	50	500
Proposed	Detection & Location	SSA	50 kHz (Detection), 1 MHz (Location)	50	500

With respect to fault location methods, the double-ended model-based technique in [23] achieves a location error of 0.8% at a 1 MHz sampling rate. Reference [27] utilizes a high-pass filter to detect wave arrival time, reaching an error of 0.145%. Although [27] emphasizes faster computation, it also acknowledges that wavelet-based approaches offer higher accuracy, which is more desirable for fault location tasks. Reference [28] accounts for variations in wave propagation velocity and reports a location error of 0.416%, while [29] presents a single-ended method using VMD with an error rate of 1.31%. Table 2 summarizes key characteristics of the referenced methods compared to the proposed SSA-based approach.

The use of a higher sampling frequency in the proposed location algorithm is aligned with previous studies [23], [28], and [29], which also rely on high-resolution sampling to reduce location error. As fault location accuracy is prioritized over computational speed in such applications, the use of a high sampling rate (1 MHz) is justified to ensure precise and reliable fault localization.

TABLE 3. Simulation results for Dc line faults, across varying fault types, impedances, and distances.

Cable	Length (m)	Fault Resistance	Fault type	IED	Actual fault distance (m)	CR	Estimated Fault Distance (m)	Error %
Line 1	7000	0.5	PP	IED12	200	1.2081325	205	0.0714286
		90	PPG		5750	0.9324884	5746	0.0571429
		190	NPG		6090	0.8973081	6093	0.0428571
Line 2	5000	0.5	PP	IED23	50	1.2081049	53	0.06
		90	PPG		2060	1.1758856	2058	0.04
		190	NPG		4600	1.0330427	4608	0.16
Line 3	7000	0.5	PP	IED34	2030	1.1770197	2024	0.0857143
		90	PPG		240	1.20809	235	0.0714286
		190	NPG		6400	0.8642027	6402	0.0285714
Line 4	5000	0.5	PP	IED25	1100	1.2001775	1094	0.12
		90	PPG		40	1.2080784	37	0.06
		190	NPG		4000	1.0773883	4001	0.02
Line 5	5000	0.5	PP	IED36	4720	1.0243951	4717	0.06
		90	PPG		320	1.2078744	323	0.06
		190	NPG		1050	1.200961	1046	0.08

H. COMPREHENSIVE ANALYSIS OF FAULT LOCATION ACCURACY AND COMPUTATIONAL COMPLEXITY IN SSA-BASED FAULT LOCALIZATION COMPARED TO OTHER METHODS

A comprehensive error analysis is conducted to compare Singular proposed SSA-based fault localization with other methods, including WT, FFT, HHT, and VMD. This analysis is performed by applying a series of test scenarios under diverse conditions, such as different fault types (e.g., Pole-to-Ground, Pole-to-Pole, and high-impedance faults). The same signal datasets are processed using each algorithm (SSA, WT, FFT, HHT, and VMD) to ensure a fair comparison.

TABLE 4. Comparison of fault localization methods: Accuracy and computational complexity across different fault scenarios.

Method	Bolted PP	PPG 40 Ω, 10 dB	NPG 110 Ω ,30 dB	PPG 200 Ω ,50 dB	Computation complexity
FFT	0.53 %	0.87	0.94	1.29	100 %
WT	0.12 %	0.19	0.33	0.46	120%
HHT	0.06 %	0.112	0.21	0.23	139%
VMD	0.06 %	0.06	0.12	0.23	142%
SSA	0.03 %	0.05	0.08	0.16	122%

Figure 17 illustrates the normalized first traveling wave (TW) for a pole-to-pole fault at 2 km away from Bus1 as an example, demonstrating that SSA produces the most pure and consistent results. The computational complexity of each algorithm (FFT, WT, HHT, VMD, and SSA) is evaluated by executing them individually on the same input dataset using a uniform computing platform (workstation with Intel Core i5 CPU and 4 GB RAM). The execution time is measured for each algorithm, with the FFT serving as the baseline due to its minimal runtime. The execution times of the other algorithms are then expressed as a percentage relative to that of the FFT. The fault location is determined in each case, and the error margin is displayed. Table 3 presents a comprehensive summary of the test case results, encompassing various fault types, fault resistance, and noise level, along with the corresponding error metrics for all evaluated scenarios.

Based on the findings presented in Fig. 17 beside Table 4, the proposed SSA-based algorithm demonstrates the highest fault location accuracy. Additionally, its computational complexity is comparable to that of the FFT method and lower than that of VMD and HHT, making it the most efficient approach overall.

V. CONCLUSION

In conclusion, this study introduces a novel fault detection, classification, and localization methodology for MT-MVDC networks, leveraging SSA to decompose pole voltage signals waves. Fault detection is performed by analyzing fluctuations in this component, while classification is determined based on the polarity of seasonal voltage values. The proposed approach demonstrates robustness against noisy measurements and eliminates the need for parameter optimization for threshold adjustments. Additionally, it effectively differentiates high-impedance faults (up to 500 Ω) from sudden load variations.

For fault localization, the method employs curvature rate analysis, utilizing traveling wave attenuation and dispersion principles to achieve precise fault identification. Unlike conventional techniques, it does not rely on wave arrival times and remains effective even under high-impedance fault conditions, achieving a maximum localization error of only 0.16%. A comprehensive comparative analysis with existing fault location schemes highlights the superior accuracy of the proposed method. Furthermore, extensive simulation studies assess its computational efficiency and fault localization performance against various signal processing techniques, including FFT, WT, HHT, and VMD. The results demonstrate that the proposed scheme achieves high accuracy while maintaining computational complexity comparable to FFT and significantly outperforming VMD and HHT in execution time. These findings validate the effectiveness of the proposed approach, establishing it as a reliable and efficient solution for fault detection and localization in MT-MVDC networks.

REFERENCES

[1] J. Valbuena Godoy, S. Negri, F. Oliva, A. Antoniazzi, and R. S. Faranda, ‘‘Innovative fault current evaluation method for active DC grids,’’ *Electronics*, vol. 13, no. 5, p. 847, Feb. 2024.

[2] J. Ke, C. Cong, Z. Qijuan, F. Tao, B. Tianshu, and L. Haijun, ‘‘Protection schemes and settings of DC distribution systems,’’ *IET Gener., Transmiss. Distrib.*, vol. 14, no. 26, pp. 6754–6762, Dec. 2020.

[3] L. Zhu, H. Zhang, H. Wang, X. Wu, Y. Shen, N. Liu, and Q. Duan, ‘‘Research on staged relay protection of DC distribution system,’’ in *Proc. IEEE 6th Conf. Energy Internet Energy Syst. Integr. (EI)*, Nov. 2022, pp. 153–161.

[4] Z. Junjie, L. Weixing, and W. Jinyu, ‘‘DC fault protection based on change rate of DC voltage in DC grid,’’ *Southern Power Syst. Technol.*, vol. 11, no. 1, pp. 14–22, 2017.

[5] B. Li, J. He, Y. Li, B. Li, and W. Wen, ‘‘High-speed directional pilot protection for MVDC distribution systems,’’ *Int. J. Electr. Power Energy Syst.*, vol. 121, Oct. 2020, Art. no. 106141.

[6] V. Nougain, S. Mishra, and A. K. Pradhan, ‘‘MVDC microgrid protection using a centralized communication with a localized backup scheme of adaptive parameters,’’ *IEEE Trans. Power Del.*, vol. 34, no. 3, pp. 869–878, Jun. 2019.

[7] Y. Li, V. Mohan, S. Jiang, Y. Wang, and J. Liang, ‘‘Wavelet transform based differential protection for MVDC distribution network,’’ in *Proc. 57th Int. Universities Power Eng. Conf. (UPEC)*, Aug. 2022, pp. 1–6.

[8] M. Li, K. Jia, T. Bi, C. Wang, R. Zhu, and Q. Yang, ‘‘Full-current-based directional pilot protection for VSC-DC distribution systems,’’ *IET Gener., Transmiss. Distrib.*, vol. 13, no. 16, pp. 3713–3724, Aug. 2019.

[9] M. Li, Y. Luo, K. Jia, T. Bi, and Q. Yang, ‘‘Frequency-based current differential protection for VSC-MVDC distribution lines,’’ *Int. J. Electr. Power Energy Syst.*, vol. 117, May 2020, Art. no. 105626.

[10] J. Duan, Z. Li, Z. Wei, and W. Lu, ‘‘A line accelerated protection scheme of flexible MVDC distribution system based on transient current derivative,’’ *Electr. Power Syst. Res.*, vol. 183, Jun. 2020, Art. no. 106269.

[11] A. Kassem, H. Sabra, A. Y. Abdelaziz, A. A. Ali, and K. M. Abdel-Latif, ‘‘Centralized event-based protection based on communication infrastructure of medium voltage direct current network,’’ *Ain Shams Eng. J.*, vol. 15, no. 6, Jun. 2024, Art. no. 102731.

[12] N. A. Larik, M. S. Li, and Q. H. Wu, ‘‘Enhanced fault detection and localization strategy for high-speed protection in medium-voltage DC distribution networks using extended Kalman filtering algorithm,’’ *IEEE Access*, vol. 12, pp. 30329–30344, 2024.

[13] K. Satpathi, Y. M. Yeap, A. Ukil, and N. Geddada, ‘‘Short-time Fourier transform based transient analysis of VSC interfaced point-to-point DC system,’’ *IEEE Trans. Ind. Electron.*, vol. 65, no. 5, pp. 4080–4091, May 2018.

[14] M. Dashtdar, Y. Belkhier, M. Bajaj, S. M. Sadegh, M. Belik, and O. Rubanenko, ‘‘Protection of DC microgrids based on frequency domain analysis using Fourier transform,’’ in *Proc. IEEE 3rd KhPI Week Adv. Technol. (KhPIWeek)*, Oct. 2022, pp. 1–6.

[15] M. Radwan and S. P. Azad, ‘‘A single-ended protection scheme for multi-terminal HVDC grids based on Hilbert–Huang transform,’’ in *Proc. IEEE Power Energy Soc. Gen. Meeting (PESGM)*, Jul. 2023, pp. 1–5.

[16] L. Liu, A. Lekic, and M. Popov, ‘‘Robust traveling wave-based protection scheme for multiterminal DC grids,’’ *IEEE Trans. Power Del.*, vol. 38, no. 5, pp. 1–13, Apr. 2023.

[17] N. K. Sharma, S. R. Samantaray, and C. N. Bhende, ‘‘VMD-enabled current-based fast fault detection scheme for DC microgrid,’’ *IEEE Syst. J.*, vol. 16, no. 1, pp. 933–944, Mar. 2022.

[18] D. Li, A. Ukil, K. Satpathi, and Y. M. Yeap, ‘‘Improved s transform-based fault detection method in voltage source converter interfaced DC system,’’ *IEEE Trans. Ind. Electron.*, vol. 68, no. 6, pp. 5024–5035, Jun. 2021.

[19] L. Jing, L. Xia, T. Zhao, and J. Zhou, ‘‘An improved arc fault location method of DC distribution system based on EMD-SVD decomposition,’’ *Appl. Sci.*, vol. 13, no. 16, p. 9132, Aug. 2023.

[20] R. G. Khuziashev, I. A. Minaev, and I. R. Tukhfatullin, ‘‘Algorithms of signal processing in traveling wave fault location complexes,’’ in *Proc. Int. Ural Conf. Electr. Power Eng. (UralCon)*, Sep. 2024, pp. 594–599.

[21] R. J. Hamidi and J. Rodriguez, ‘‘A source-independent fault detection method for transmission lines,’’ 2024, *arXiv:2409.07439*.

[22] A. A. Jabbar, M. Z. C. Wanik, and A. P. Sanfilippo, ‘‘Power quality analytical methodology using signal processing and machine learning techniques for grid fault classification and location detection,’’ in *Proc. IEEE 12th Int. Conf. Smart Energy Grid Eng. (SEGE)*, Aug. 2024, pp. 52–56.

[23] J. Xu, Y. Lü, C. Zhao, and J. Liang, ‘‘A model-based DC fault location scheme for multi-terminal MMC-HVDC systems using a simplified transmission line representation,’’ *IEEE Trans. Power Del.*, vol. 35, no. 1, pp. 386–395, Feb. 2020.

[24] A. Hadaeghi, M. M. Iliyaeifar, and A. A. Chirani, ‘‘Artificial neural network-based fault location in terminal-hybrid high voltage direct current transmission line,’’ *Int. J. Eng.*, vol. 36, no. 2, pp. 215–225, 2023.

[25] S. Salehimehr, S. M. Miraftabzadeh, and M. Brenna, ‘‘A novel machine learning-based approach for fault detection and location in low-voltage DC microgrids,’’ *Sustainability*, vol. 16, no. 7, p. 2821, Mar. 2024.

[26] S. Jiang, ‘‘Traveling wave protection of medium voltage DC distribution network,’’ in *Proc. 16th Annu. Conf. China Electrotechnical Soc.*, vol. 2. Singapore: Springer, 2022, pp. 1208–1215.

[27] S. Javaid, D. Li, and A. Ukil, ‘‘High pass filter based traveling wave method for fault location in VSC-interfaced HVDC system,’’ *Electric Power Syst. Res.*, vol. 228, Mar. 2024, Art. no. 110004.

[28] Z. Liu, K. Zhang, J. Zhang, S. Shi, H. Liu, and X. Dong, ‘‘Improved double-ended traveling wave ranging technology for DC distribution cable lines,’’ *J. Phys., Conf. Ser.*, vol. 2495, no. 1, May 2023, Art. no. 012023.

[29] Q. Huai, K. Liu, A. Hooshyar, H. Ding, K. Chen, and Q. Liang, ‘‘Single-ended line fault location method for multi-terminal HVDC system based on optimized variational mode decomposition,’’ *Electr. Power Syst. Res.*, vol. 194, May 2021, Art. no. 107054.

[30] W. Wan, Z. Qin, M. Deng, and Y. Liu, ‘‘Traveling wave network location method based on adaptive waveform similarity,’’ *Heliyon*, vol. 10, no. 18, Sep. 2024, Art. no. e37576.

[31] N. Neeraj, J. Mathew, M. Agarwal, and R. K. Behera, ‘‘Long short-term memory-singular spectrum analysis-based model for electric load forecasting,’’ *Electr. Eng.*, vol. 103, no. 2, pp. 1067–1082, Apr. 2021.

[32] V. Abolghasemi, M. H. Marzebali, and S. Ferdowsi, ‘‘Recursive singular spectrum analysis for induction machines unbalanced rotor fault diagnosis,’’ *IEEE Trans. Instrum. Meas.*, vol. 71, pp. 1–11, 2022.

[33] H. Al-Bugharbee and I. Trendafilova, ‘‘A new methodology for fault detection in rolling element bearings using singular spectrum analysis,’’ *Int. J. Condition Monitor.*, vol. 7, no. 2, pp. 26–35, May 2017.

[34] D. S. Broomhead and G. P. King, ‘‘Extracting qualitative dynamics from experimental data,’’ *Phys. D, Nonlinear Phenomena*, vol. 20, nos. 2–3, pp. 217–236, Jun. 1986.

[35] N. Golyandina, V. Nekrutkin, and A. A. Zhigljavsky, *Analysis of Time Series Structure: SSA and Related Techniques*. Boca Raton, FL, USA: CRC Press, 2001.

[36] F. V. Lopes, J. P. G. Ribeiro, T. R. Honorato, K. M. Silva, J. N. Rezende Jr., C. A. M. Aviz, and R. O. Fernandes, ‘‘Time-domain relay performance evaluation considering Brazilian fault cases,’’ in *Proc. Int. Conf. Power Syst. Transients (IPST)*, Perpignan, France.

HOSSAM SABRA was born in Gharbia, Egypt, in 1987. He received the B.Sc. degree in electrical engineering from Tanta University, Egypt, in 2009, and the M.Sc. degree in electrical engineering from Cairo University, Egypt, in 2017.

He was a Protection and Maintenance Engineer with South Cairo Electricity Distribution Company, from 2010 to 2019, with a focus on medium-voltage network protection, testing, and commissioning. Since 2019, he has been an Advanced Distribution Management System (ADMS) Engineer, specializing in ADMS platform for grid optimization, outage restoration, and SCADA integration. He is currently an experienced Electrical Engineer specializing in power distribution and network optimization. He has made significant contributions to the field of power distribution and smart grid technologies. His research interests include power system protection, distribution network automation, and renewable energy integration.

AMR KASSEM was born in Cairo, Egypt, in 1986. He received the B.Sc., M.Sc., and Ph.D. degrees in electrical engineering from Helwan University, Cairo, in 2008, 2012, and 2019, respectively. His research focuses on renewable energy integration in smart grids, the IoT applications in power systems, digital relaying, and microgrid protection.

AHMED A. A. ALI (Member, IEEE) was born in Saudi Arabia, in 1978. He received the B.Sc. degree in electrical power and machines engineering and the M.Sc. degree in electric power and machines engineering (power electronics) from Helwan University, Egypt, in 2000 and 2007, respectively, and the Ph.D. degree in electrical power and machines engineering from Helwan University in partnership with the University of Calgary, Canada, in 2014, specializing in renewable energy.

He was promoted to an Associate Professor in 2020 and subsequently served as the Head of the Electrical Power and Machines Engineering Department at Helwan University from 2020 to 2022. In 2025, he attained the rank of Full Professor. He currently holds the title of certified Consultant with the Engineers Syndicate, Cairo, Egypt. He has over 24 years of experience in electrical power engineering consulting and project management. He has managed projects, programs, and portfolios, leading and supervising electrical teams in developing conceptual designs and technical studies for wind and photovoltaic integration projects. His expertise includes mid- and long-term planning and operational technical solutions for power system reliability and compliance with applicable standards. He has authored more than 40 scientific research papers in international journals and conferences. Additionally, he has participated in several international funded research projects, including AIP, ERECI, and SEM-SEM, and is involved in InVivo nEXTh and MEDSOL. His research interests include distributed generation management systems for large-scale utilities, energy management systems for wind and tidal energy conversion, and power system operation and planning.

KARAM M. ABDEL-LATIF was born in Cairo, Egypt, in 1971. He received the B.Sc., M.Sc., and Ph.D. degrees in electrical engineering from Helwan University, Egypt, in 1995, 2002, and 2009, respectively.

He began his academic career as a Demonstrator with the Department of Electrical Power and Machines Engineering, Helwan University, in 1995, before being promoted to an Assistant Lecturer, in 2001. In March 2009, he was appointed as an Assistant Professor and later advanced to an Associate Professor, in 2016. He was promoted to a Full Professor, in 2024. As part of his Ph.D. studies, he conducted research with the University of Calgary, Canada, in 2007. He has extensive experience in power system engineering, consulting, and research. His expertise includes microgrids, renewable energy, digital relaying, power system protection, smart cities, and the integration of wide-area networking in power systems. He was a Consultant on numerous projects across Middle East, with a focus on strategic planning and electrical infrastructure design for new cities and villages.

AHMED F. ZOBAA (Senior Member, IEEE) received the B.Sc. (Hons.), M.Sc., and Ph.D. degrees in electrical power and machines from Cairo University, Egypt, in 1992, 1997, and 2002, respectively, and the Doctoral of Science degree from the Brunel University of London, U.K., in 2017. He was an Instructor from 1992 to 1997, a Teaching Assistant, from 1997 to 2002, and an Assistant Professor, from 2002 to 2007 with Cairo University, Egypt. From 2007 to 2010, he was a Senior Lecturer in renewable energy with the University of Exeter, U.K. From 2010 to 2019, he was a Senior Lecturer in power systems with the Brunel University of London. He is currently a Reader in electrical and power engineering and a member of the Brunel Interdisciplinary Power Systems Research Centre, Brunel University of London. He received his Postgraduate Certificate in Academic Practice from the University of Exeter, in 2010. His main areas of expertise include power quality, (marine) renewable energy, smart grids, energy efficiency, and lighting applications. He is an editorial board member, an editor, an associate editor, and an editorial advisory board member of many international journals. He is also a Registered Member of the Engineering Council, U.K., Egypt Syndicate of Engineers, and Egyptian Society of Engineers. He is a Principal Fellow of the Higher Education Academy, U.K., a fellow of the Institution of Engineering and Technology, Energy Institute, U.K., the Chartered Institution of Building Services Engineers, U.K., the Institution of Mechanical Engineers, U.K., the Royal Society of Arts, U.K., and African Academy of Sciences. He is the Executive Editor-in-Chief of *Smart Grids and Sustainable Energy*. He is a registered chartered engineer, a chartered energy engineer, an European engineer, and an international professional engineer.

• • •